Journal of Ovonic Research Vol. 15, No. 4, July – August 2019, p. 247 - 260

STRUCTURAL, THERMAL AND OPTICAL ANALYSES OF COBALT-DOPED CdO THIN FILMS

M. M. MAHASEN[a], M. M. SORAYA[a], EL S. YOUSEF[b,c],
GOMAA A. M. ALI[d,e], E. R. SHAABAN[f,*]
[a]*Physics Department, Faculty of Science, Aswan University, Aswan, Egypt*
[b]*Research Center for Advanced Materials Science (RCAMS), King Khalid University, Abha 61413, P. O. Box 9004, Saudi Arabia*
[c]*Physics Dep., Faculty of Science, King Khalid University, P. O. Box 9004, Abha, Saudi Arabia*
[d]*Chemistry Department, Faculty of Science, Al-Azhar University, Assiut, 71524, Egypt*
[e]*Faculty of Industrial Sciences & Technology, Universiti Malaysia Pahang, Gambang, 26300 Kuantan, Malaysia*
[f]*Physics Department, Faculty of Science, Al-Azhar University, Assiut, 71542, Egypt*

Cadmium oxide (CdO) nanoparticles and cobalt (0.025, 0.050, 0.075, and 0.100) doped CdO were synthesized by co-precipitation method. The thermal properties were investigated by thermogravimetric analysis and differential thermogravimetric for identifying the calcination temperature of the obtained nanoparticles of pure and Co-doped CdO. The microstructure parameters were deduced by the assistant of X-ray diffraction technique, in which the particle size and the microstrain decrease with increasing Co concentration. The findings, derived from Scherrer method, Williamson-Hall models and size-strain plot analyses, confirmed Co doping into the CdO host lattice. Examination of optical absorption viewed that as Co concentration increase, the energy gap increases, attributed to the merging of Fermi level into the conduction band with the addition of carrier concentration (Moss-Burstein shift effect) and hence blocked the low energy transitions. The increase in band gap may also be assigned to the decrease in grain size.

(Received April 29, 2019; Accepted August 15, 2019)

Keywords: Nanoparticles, Precipitation method, Co-doped CdO, XRD analysis, FTIR, TEM, Optical absorption

1. Introduction

Recently, transparent conducting oxide materials subjected to intensive research due to their promising properties of transporting electric charge and transmitting photon in the visible range; that can be used in technological devices [1, 2]. CdO is a promising transparent conducting oxide (TCO) due to its high electrical conductivity ($>10^3\ \Omega^{-1}\ \mathrm{cm}^{-1}$) [3], direct band gap of 2.2 eV [4] and it has a non-stoichiometric composition, that is because of the presence of cadmium interstitials [5] or oxygen vacancies [6] acting as donors [7]. In addition, high optical transmittance in the visible region of electromagnetic spectrum [8, 9], and high reflectance in the infrared region [10]. Owning to its virtual properties, low cost and high chemical stability, CdO used in different applications such as; photovoltaic devices [11], [12], gas sensors [13], phototransistors and diodes [14], transparent electrodes [2, 15] and other applications. The introduction of cobalt, which is a transition magnetic metal element, to CdO, lead to astonishing optical, electrical and magnetic properties. This mainly because of the interaction between the band electrons and the cobalt magnetic ion within CdO lattice.

The present study aimed to prepare pure and Co-doped CdO by co-precipitation method. The samples were characterized by thermogravimetric analysis (TGA) and differential

---

[*]Corresponding author: esam_ramadan2008@yahoo.com

thermogravimetric (DTA), X-ray diffraction (XRD), transmission electron microscopy (TEM), energy dispersed X-ray (EDX) and Fourier transform infrared (FTIR) spectroscopy techniques. Moreover, the effect of cobalt doping on the crystal structure and optical properties were discussed in detail. As far as we know, explanatory structural research on pure and Co-doped CdO samples using the various Williamson-Hall (W–H) models (UDM, USDM, and UDEDM), size–strain plot (SSP) analyses and TEM, has not been reported yet. More accurate evaluation of the different structural parameters were obtained for pure and Co-doped CdO nanoparticles in this study.

2. Experimental procedure

2.1. Method and materials preparations

The bulk samples of $Cd_{1-x}Co_xO$ (x = 0.000, 0.025, 0.050, 0.075, and 0.100) were prepared by using co-precipitation technique. The chemical reagents used in the synthesis of samples were analytical grade (Sigma-Aldrich). In a typical procure, a mixture of $Cd(NO_3)_2.6H_2O$ with the appropriate amount of $Co(NO_3)_2.6H_2O$ to make desired doping percentage dissolved in 50 mL of distilled water and then kept stirring for 1 h to get a clear solution. NH_4OH solution was added dropwise to the mixture until the pH of the solution reached 9. This mixture was stirred for 3 h at room temperature, consequently, filtered. The precipitate was dried at 80 ^oC for 5 h. Finally, the dried samples were grounded and kept for calcination at 480 ^oC for 2 h, to form a polycrystalline powder.

2.2. Materials characterizations

The thermal behavior of the precursors was characterized by thermogravimetric analysis (Shimadzu 50 with an accuracy of ±0.1 K) from 25-700 °C. To study the crystal structure of the synthesized materials, XRD was carried out using Philips X-ray diffractometer (model-X′pert) employing Cu-K_α radiation (λ= 1.54056 Å). XRD patterns are scanned at a rate of degree/0.6 sec with a step size of 0.02^o within a range of 10^o to 70^o. TEM was carried out by (JEOL-2010) to identify the morphologies of the samples. FTIR spectra were recorded at room temperature using Shimadzu FTIR spectrometer in the mid-infrared range of 400–4000 cm^{-1}. The optical properties of the samples were studied using UV-Vis-NIR double beam spectrophotometer (JASCO, V-670). The absorption spectra of samples were recorded in the range of 190–2500 nm for a dispersed solution (powder dispersed in ethanol) using Quartz cuvette with a thickness of 1 cm.

3. Results and discussions

Fig. 1 shows the TGA/DTG curves for the as-prepared CdO and $Cd_{0.9}Co_{0.1}O$ samples in the temperature range of 30–700 °C. The differentiation of TGA was used here to distinguish the peaks with high precision. It is clear that the behavior of the two samples is quite the same, despite the slight difference in the characteristic temperature range. Two weight losses stages were detected, the first stage starts in the two materials at about 150 ^oC which is corresponding to the first endothermic peak in the differentiation plot at exactly 202.7 ^oC in Fig. 1a and 212.5 ^oC in Fig. 1b, and the weighting loss percent is 10% for pure CdO and 6.5% for $Cd_{0.9}Co_{0.1}O$. This first loss in weight could be assigned to the evaporation of water and organics. The second decomposition stage starts at about 230 ^oC and ends with a plateau at about 400 ^oC. The second endothermic peak in the differentiation plot is exactly at 311.2 ^oC in Fig. 1a and at 317.1 ^oC in Fig. 1b, and the weighting loss percent is about 7% for pure CdO and $Cd_{0.9}Co_{0.1}O$. This second weight loss could be attributed to the conversion of the precursor's materials to the crystalline phase of pure CdO and $Cd_{0.9}Co_{0.1}O$. After 400 ^oC no weight loss was observed which mean the decomposition process is completed [16] [17] [18]. Therefore, the dried samples were calcinated at 400 ^oC for 4 h to obtain a crystalline powder. The diffraction patterns of the synthesized pure and Co-doped CdO samples are shown in Fig. 2. It illustrates that those patterns belong to the cubic phase of CdO with a lattice parameter a = 4.6960 Å and Fm_3m space group. The peaks of pure CdO at 2θ values of 33.24^o, 38.48, 55.44, 66.00 and 69.52° are corresponding to the Miller indices of (111), (200), (220), (311) and (222), respectively. The XRD patterns of the doped CdO showed similar peaks with the increase of the cobalt ratio indicating that all $Cd_{1-x}Co_xO$ samples had the form of monophasic highly crystalline cubic CdO structure. No other peaks of any secondary or impurity phases with the addition of Co in CdO samples were observed implying that Co particles are incorporated interstitially instead of forming a new phase. Fig. 3 represents an improvement in the crystallization quality with Co incorporation in CdO samples that would result in increase in the peak intensity of CdO planes without any shift in their peak positions. The corrected value of lattice parameter a (Å) for Co-doped CdO samples were calculated using Nelson-Riley plot as shown in Fig. 4, in which the lattice parameter a (calculated from the Bragg's law) was plotted against the following extrapolation function f(θ) [19]:

$$f(\theta) = \frac{1}{2}\left(\frac{\cos\theta^2}{\sin\theta} + \frac{\cos\theta^2}{\theta}\right) \tag{1}$$

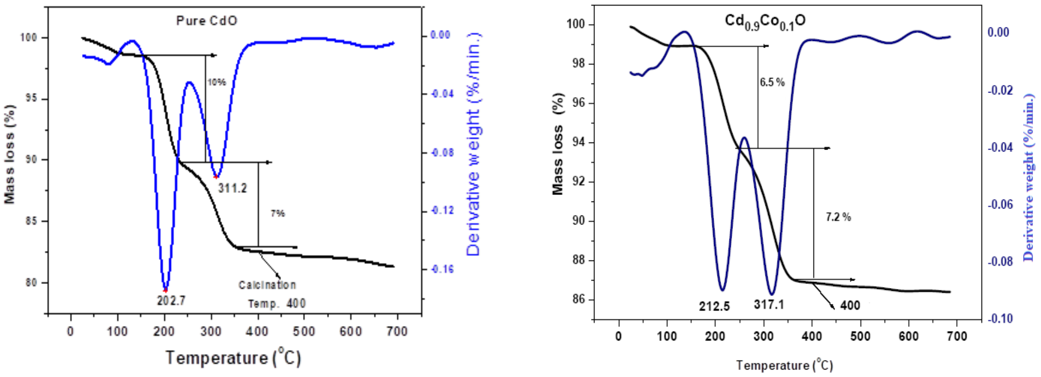

Fig. 1. TGA/DTG curves of (a) pure CdO and (b) $Cd_{0.9}Co_{0.1}O$ precursors.

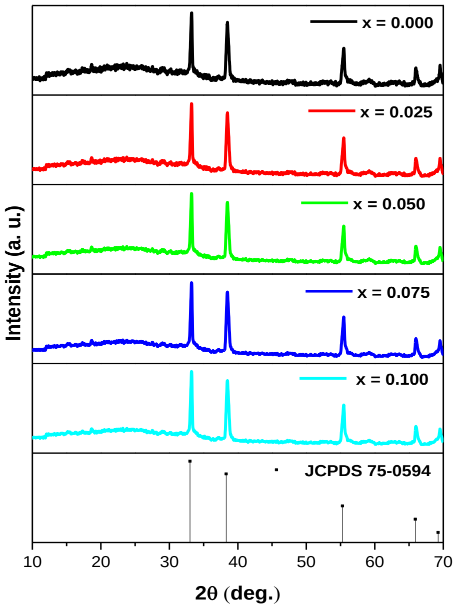

Fig. 2. XRD patterns of $Cd_{1-x}Co_xO$ samples.

The estimated values of the lattice parameter for all Co-doped CdO samples is 4.69829 Å, which is close to the standard value of 4.6960 Å according to the card (JCPDS75–0594). The absence of any shift in the position of the main peaks (Fig. 3) for Co-doped sample, resulting in that all d_{hkl} values corresponding to the *hkl* planes are not altering by cobalt doping. Consequently, all the values of the lattice parameters would be the same. Moreover, increasing of Co doping percentage result in increasing the peaks intensity and peaks broadening. Therefore, the crystallite size (*D*) was estimated from the Debye-Scherrer equation:

$$D = \frac{K\lambda}{\beta_{hkl}\ \cos\theta} \tag{2}$$

where *K* is shape factor (0.9), and λ is the wavelength of the used Cu-K$_\alpha$ radiation (λ = 1.54056 Å), θ the scattering angle at maximum peak and β_{hkl} is the full width at half maximum (FWHM) corrected for instrumental broadening ($\beta_{hkl} = [(\beta)^2_{measured} - (\beta)^2_{instrument}]^{0.5}$. The crystallite size estimated by considering the average of the crystallite sizes obtained for the five main peaks. The calculated average crystallite size was in the range of 26.65–21.81 nm for the pure and Co-doped CdO nanoparticles as listed in Table 1. The crystalline size decrease with the increasing of cobalt percent in the CdO crystal due to small grain growth of Co-doped CdO as compared to pure CdO nanoparticle which has a good agreement with the literature [20] for Co-doped CdO. A dislocation is an imperfection in a crystal and the dislocation density (δ) is the density of defects or the length of dislocation lines per unit volume of the crystal, it could be calculated from Williamson and Smallman's formula: $\delta = 1/D^2$, Thus, the calculated δ for Co-doped CdO increased with the increase of CO percent as shown in Table 1.

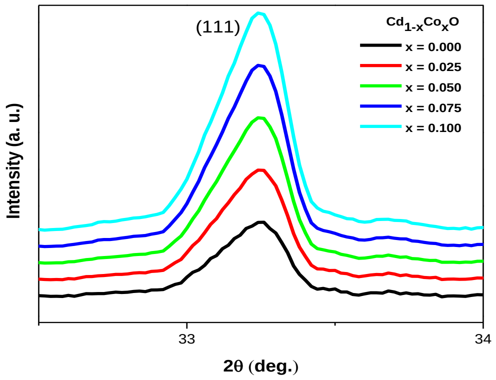

Fig. 3. Focusing view of the peak corresponding to (111) plane in XRD patterns of Cd$_{1-x}$Co$_x$O.

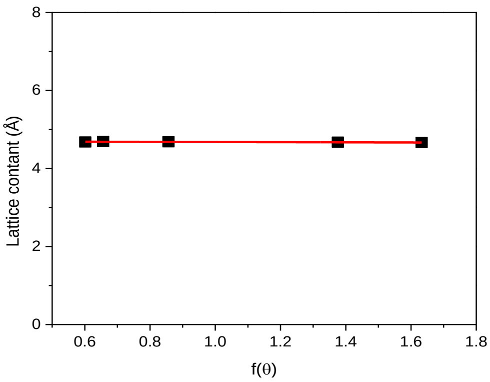

Fig. 4. The relation between the lattice parameter and f(θ).

Table 1. Geometric parameters of $Cd_{1-x}Co_xO$ nanoparticles ay Cobalt concentrations.

Concentration of Cobalt (at%)	Scherrer method	dislocation density	Stokes −Wilson	Williamson-Hall method									Size-Strain Plot method				TEM
				UDM		USDM			UDEDM								
	$D(nm)$	$\delta x10^{-3}$ (nm^{-2})	$\varepsilon x10^{-3}$	$D(nm)$	$\varepsilon x10^{-3}$	$D(nm)$	$\varepsilon x10^{-3}$	$\sigma(MPa)$	$D(nm)$	$\varepsilon x10^{-3}$	$\sigma(MPa)$	$u(KJm^{-3})$	$D(nm)$	$\varepsilon x10^{-3}$	$\sigma(MPa)$	$u(KJm^{-3})$	$D(nm)$
0	26.65	1.41	5.05	29.44	2.15	29.19	2.13	313.99	29.31	2.14	315.64	338.19	12.38	15.75	2319.58	18263.61	23.98
0.025	25.19	1.58	5.37	24.85	1.95	24.67	1.93	283.61	24.76	1.94	285.09	275.89	11.05	15.46	2276.97	17598.91	-
0.05	23.95	1.74	5.69	20.94	1.63	20.85	1.61	237.6	20.88	1.62	238.75	193.49	9.62	13.77	2028.03	13961.01	-
0.075	23.01	1.89	5.93	19.84	1.64	19.78	1.63	239.56	19.81	1.63	240.64	196.56	9.15	13.96	2056.68	14358.3	-
0.1	21.81	2.1	6.31	17.05	1.32	17.01	1.31	192.52	17.03	1.31	193.44	127.01	8.26	12.96	1909.59	12378.04	17.28

However, the peak broadening in the XRD not only due to finite crystallite (grain) size but also the presence of the stress inside the crystal causing strain, i.e. grain size and microstrain effects are interconnected in the line broadening of peak and difficult to separate them. Lattice strain broadening is caused by varying displacement of the atoms with respect to their reference-lattice positions. the induced microstrain (ε) could be estimated using Stokes–Wilson equation [21]. The calculated ε for the Co-doped CdO are listed in Table 1.

$$\varepsilon = \frac{\beta_{hkl}}{4\tan\theta} \tag{3}$$

Many attempts reported to separate and evaluate the size and strain parameters from the occurring line broadening such as Variance method, Warren-Averbach method ref and W–H analysis among them, W–H method is a simplified approach to deconvolute strain and finite size induced broadening. In the W–H approach, crystallite size (Scherrer considerations) and strain effects (Wilson equation). The former varies with respect to 1/cosθ and the latter varies with respect to tan θ, related broadening as the following equation [22]:

$$\beta_{hkl} = \beta_D + \beta_\varepsilon \tag{4}$$

$$\beta_{hkl} = \frac{\mathrm{K}\,\lambda}{\mathrm{D}\cos\theta_{hkl}} + 4\varepsilon\tan\theta_{hkl} \tag{5}$$

$$\beta_{hkl}\cos\theta_{hkl} = \frac{\mathrm{K}\,\lambda}{\mathrm{D}} + 4\varepsilon\sin\theta_{hkl} \tag{6}$$

The micro-strain can be calculated from the slope of (Fig. 5) the plot of $\beta_{hkl}\cos\theta_{hkl}$ on the y-axis against $4\sin\theta_{hkl}$ on the x-axis and the crystallite size from the intercept of Y-axis. The calculated parameters for the Co-doped CdO samples are listed in Table 1. However, Eqs. 9 and 10 assuming a uniform deformation model (UDM), meaning they assume that the crystal is of isotropic nature, and the strain ε to be uniform in all crystallographic directions. For a crystalline material, this assumption is questionable. It is more proper to consider an anisotropic strain ε_{hkl}.

A summarized view of the structural parameter deduced from Scherrer and W-H formulas with the increase in Co percentage is shown in Fig. 6. As the Co concentration increases both *D* (Scherrer and W-H) and the *ε* decrease and the dislocation density increases, this may be observed due to the replacement of Cd ions by Co ions.

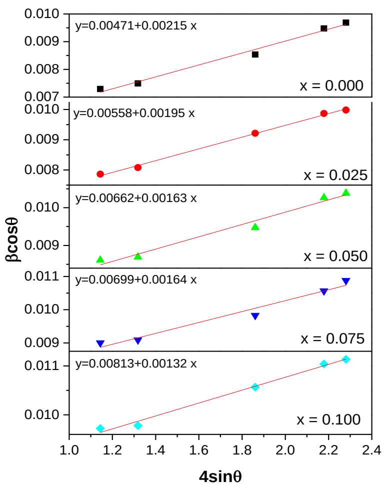

Fig. 1. Williamson-Hall plot of nanocrystalline $Cd_{1-x}Co_xO$ samples, assuming uniform deformation model.

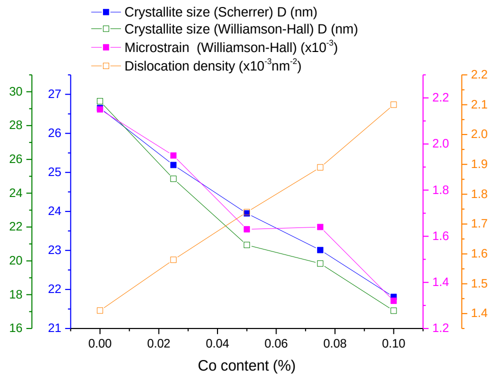

Fig. 2. Crystallize size (using Scherrer and W-H formulas), lattice strain and dislocation density as a function of Co content.

3.1. Uniform stress deformation model

In assuming the uniform stress (deformation pressure) (σ) [23], the isotropic strain (ε) in Eqs. 8 and 10 is replaced by an anisotropic strain $\varepsilon_{hkl} = \sigma/E_{hkl}$. Where E_{hkl}, the constant of proportionality, is the modulus of elasticity or Young's modulus in the direction perpendicular to the *hkl* plane. This relation represents Hook`s law, in which the stress is linearly proportional to the strain, within the elastic limit. The lattice deformation stress is isotropic and this relation only valid for the significantly small strain. W–H equation would be modified by utilizing the UDSM model, as follows:

$$\beta_{hkl}\cos\theta_{hkl} = \frac{\mathrm{K}\,\lambda}{\mathrm{D}} + \frac{4\sigma\sin\theta_{hkl}}{E_{hkl}} \tag{7}$$

Young`s modules are calculated from the following equation for cubic crystal structural, and the sample elastic compliances [24].

$$\frac{1}{E_{hkl}} = S_{11} - 2\left(S_{11} - S_{12} - \frac{1}{2}S_{44}\right)\frac{(hk)^2 + (hl)^2 + (kl)^2}{(h^2 + k^2 + l^2)^2} \tag{8}$$

where, S_{11}, S_{12} and S_{44} are the elastic compliances.

The elastic compliances S_{ij} and the elastic constants C_{ij} [25] used in this study for the CdO samples are illustrated in Table 2. For cubic structures, the elastic compliances S_{ij} and the elastic constants C_{ij} are connected as follows [26]:

$$S_{11} = \frac{C_{11} + C_{12}}{(C_{11} - C_{12})(C_{11} + 2\,C_{12})} \tag{9}$$

$$S_{12} = -\frac{C_{12}}{(C_{11} - C_{12})(C_{11} + 2\,C_{12})} \tag{10}$$

$$S_{44} = \frac{1}{C_{44}} \tag{11}$$

After calculating Young`s modulus and plotting the values of $\beta_{hkl}\ cos\theta_{hkl}$ in the y-axis against that of $4sin\theta_{hkl}/E_{hkl}$ in the x-axis in Fig. 7, using Eq. 12, the uniform deformation stress can be estimated from the slope of the linearly fitted line and consequently the value of lattice strain could be derived, furthermore the crystallite size could be found from the y-intercept (Table 1).

Table 2. The CdO elastic compliances S_{ij} and elastic constants C_{ij}.

Elastic compliances (m^2/N, or Pa) *Cubic crystal (CdO)*			
C_{11}	218.6	S_{11}	6.68×10^{-12}
C_{12}	105.6	S_{12}	-2.17×10^{-12}
C_{44}	54.9	S_{44}	18.21×10^{-12}
Ref.	[25]		

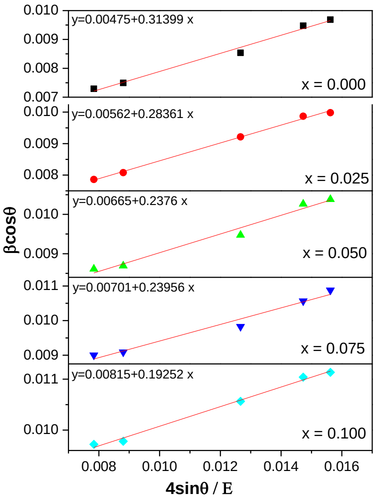

Fig. 3. Williamson-Hall plot of nanocrystalline $Cd_{1-x}Co_xO$ samples, assuming uniform stress deformation model (USDM).

3.2. Uniform deformation energy density model

In USD model, the lattice strain was assumed to be anisotropic while the deformation to be isotropic. In this type of modification on W–H equation, both the lattice deformation stress and the strain are anisotropic since the homogeneity and isotropy of nanocrystalline materials is not a realistic assumption. But another parameter called the density of deformation energy is isotropic. Also, using Hook's law the deformation energy u (energy per unit volume) is connected to the strain as $u = \frac{\varepsilon_{hkl}^2 E_{hkl}}{2}$.

Hence, assuming this density to be uniform and substitute the new anisotropic strain in Eq. 11, the resulted modified W-H equation presented as the following:

$$\beta_{hkl}\cos\theta_{hkl} = \frac{\mathrm{K}\,\lambda}{\mathrm{D}} + 4\sin\theta_{hkl}\left(\frac{2u}{E_{hkl}}\right)^{\frac{1}{2}} \tag{12}$$

Drawing this equation and, linearly fitting the values of $\beta_{hkl}\cos\theta_{hkl}$ on the y-axis and that of $4\sin\theta_{hkl}\left(\frac{2}{E_{hkl}}\right)^{\frac{1}{2}}$ on the x-axis illustrated in Fig. 8, the uniform deformation energy density, and the crystallite size is deduced from the slope and the y-intercept of the line, respectively.

Additionally, the lattice strain calculated from $\varepsilon_{hkl} = \sqrt{\frac{2u}{E_{hkl}}}$ (Table 1). From the different plots of the W–H equation, a particular sample may result in different values for the lattice strain and the crystallite size. W–H plots could be drawn by utilizing any equation from the previous Eqs. 11, 12 or 17, and the most suitable model would be chosen as the W-H model, which represent the best fit of the experimental data.

3.3. Size–strain plot

The W–H showed that line broadening was essentially isotropic. This indicates that the diffracting domains were isotropic and there was also a strain contribution. But with the presence of anisotropic line broadening, using the SSP for determining the average crystallite size and lattice strain is more accurate. Having the advantage that the data for reflections at low and intermediate angles are given more weight than those at higher angles (meaning not fully depend on the data from reflections at high angles), for which broadening are usually determined with less precision. The size–strain plot equation is illustrated as follows [27]:

$$(d_{hkl}\beta_{hkl}\cos\theta_{hkl})^2 = \frac{K}{D}(d_{hkl}^2\beta_{hkl}\cos\theta_{hkl}) + \left(\frac{\varepsilon}{2}\right)^2 \tag{13}$$

where, K is a constant which its value depends on the particle shape, for spherical particles is equals to 3/4. That equation assumes the size and strain profiles are Lorentzian and Gaussian, respectively. Plotting $(d_{hkl}\beta_{hkl}\ cos\theta_{hkl})^2$ versus $(d^2_{hkl}\beta_{hkl}\ cos\theta_{hkl})$ for the all orientation peaks and angles and then linearly fitting the resulted line as done in Fig. 9. The slope would give the crystal size and the y-intercept would give rise to the strain. All the results obtained from the Scherrer method, W–H models (UDM, USDM, and UDEDM) and SSP analyses are summarized in Table 1. In Table 1 the crystallite sizes estimated from the Scherrer method were lower than the ones from W–H method. These results are normal considering that Scherrer method do not take the effect of strain in X-ray peak broadening and that would, in turn, affect the estimation of crystallite size. For that reason, W–H method is more accurate than the Scherrer method. On the other hand, W–H method with its various modified models that each assume different natures of crystallite, no sizeable difference could be observed in strain. Under different conditions, the SSP method calculated strain values are much higher than the W–H method ones. That major observed difference could be regarded to the lower angle contributions in the SSP method. The scattering of the points away from the linear expression fitting line is much less for Fig. 9 as compared with Figs. 6, 7 and 8. Because of that the size–strain plot method was established to be more suitable for the studied $Cd_{1-x}Co_xO$ samples.

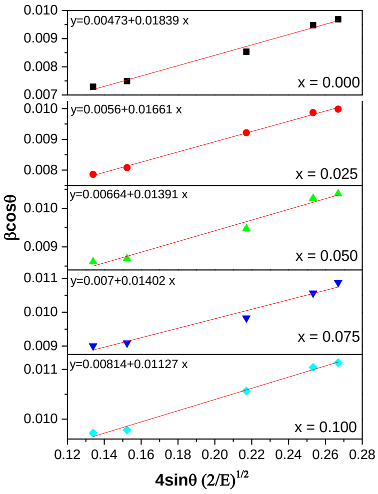

Fig. 4. Williamson-Hall plot of nanocrystalline $Cd_{1-x}Co_xO$, assuming uniform deformation energy density model (UDEDM).

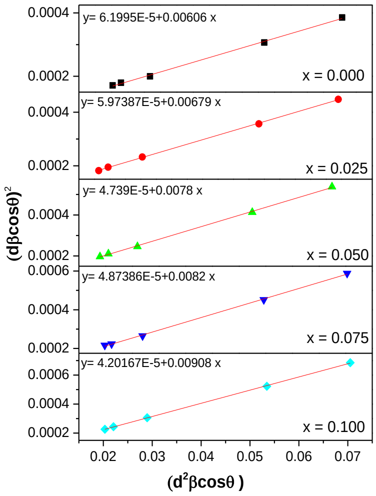

Fig. 5. Size–strain plots of $Cd_{1-x}Co_xO$ *samples.*

However, the XRD technique provides rich and reliable information about crystallite sizes, due to the large irradiated volume. Another method to characterize the grain size is TEM [28], which present less information than XRD, because it concentrates on only a local area of the sample. However, it provides a direct way to view the grain size. For those reasons, both XRD and TEM are complementary to each other. In both TEM images in Fig. 10, the CdO nanoparticles aggregated because of the high surface energy of the growth particles in nanoscale. Also, the agglomeration in the pure CdO (Fig. 10a) is more that of $Cd_{0.9}Co_{0.1}O$ (Fig. 10b). The calculated average particle size from the distribution curves was found to be 23.98±5.28 and 17.28±3.37 nm for the CdO and $Cd_{0.9}Co_{0.1}O$, respectively. The crystallite sizes obtained from the XRD (using SSP method) are smaller than the particle sizes obtained from the TEM due to the particle size compose of more than one crystallite, this may lead to the above observation. which matched with the literature [29-32]. To study characteristic functional groups of the samples, FTIR spectra were recorded in the range of 400-4000 cm^{-1} as presented in Fig. 11. The broad FTIR absorption band at 3463, 3455, 3429 and 3389 cm^{-1} is assigned to stretching vibrational mode of a hydroxyl group O–H [33] for Co-doped CdO samples, which is due to the water molecules occluded in the solid [34, 35]. The absorption bands at 2331, 2330, 2330, 2332 and 2332 cm^{-1} are a consequence of the presence of atmospheric carbon dioxide O=C=O [34, 36]. That presence of water and carbon dioxide is a normal result since the used KBr pellet was formed at room temperature and without vacuum. The bands at 2920, 2919 and 2921 cm^{-1} are assigned to asymmetric and symmetric stretching modes of C-H group [33] [37]. The peaks at 1672, 1666, 1678 and 1692 cm^{-1} are assigned to C=O and the ones at 1331, 1362, 1482, 1470 and 1456 cm^{-1} corresponds to O-C-O and those absorption bands are the symmetric stretching vibrations of the carbonyl group [38]. For CdO the absorption band at 659 cm^{-1} is corresponds to (Cd-O) [37], [39], since the characteristic band of CdO in the range of 700-625 cm^{-1} [40]. while in the Co-doped CdO curves, the peaks found to be at 672, 775, 777 and 777 cm^{-1}, these peaks are assigned to stretching Co-O [34] and to Cd-O [37], [39].

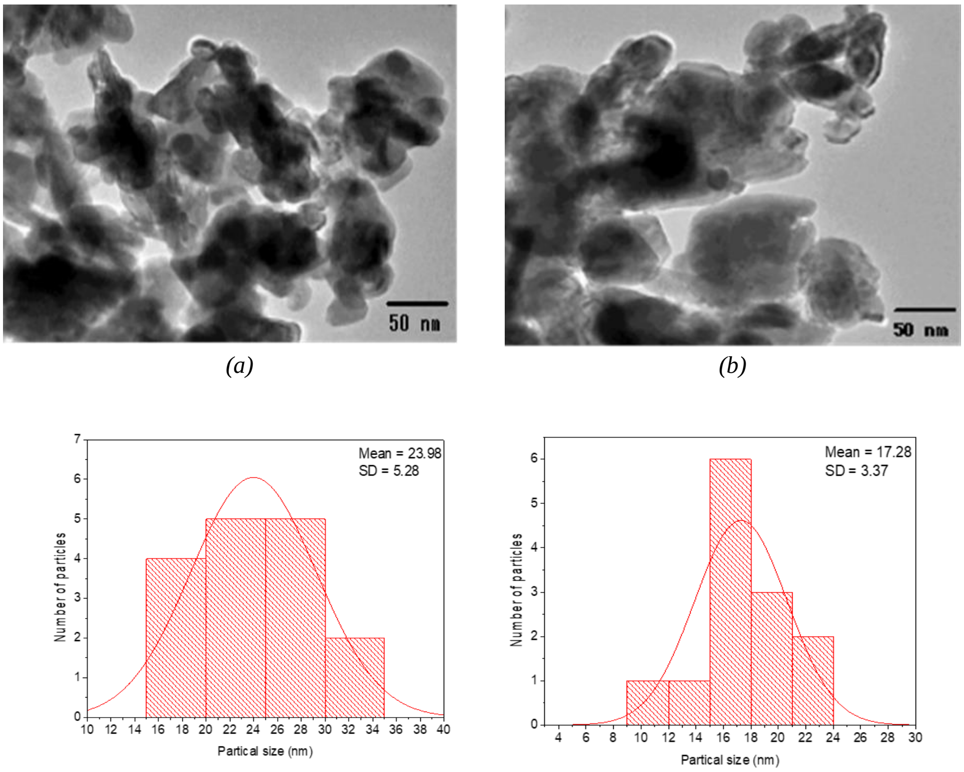

(a) *(b)*

(c) *(d)*

Fig. 6. Representative TEM micrographs (a and b) and particles size distributions (c and d) for CdO and (b) $Cd_{0.9}Co_{0.1}O$ nanoparticles, respectively.

Finally, the overall view of the curves in Fig. 11 are similar, with the difference in intensity decreasing with increasing Co doping percent. The other observation is the slight shift of peaks toward higher energy side also with increasing the Cobalt. That can be attributed to the incorporation of Co^{2+} ions in the Cd crystal lattice.

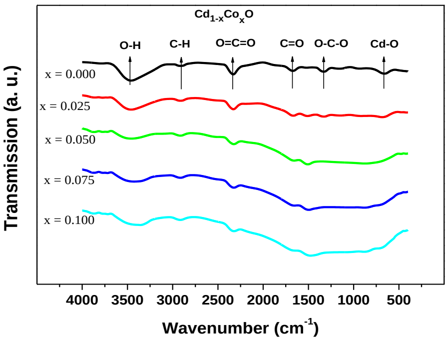

Fig. 7. FTIR spectra of CdO and $Cd_{1-x}Co_xO$ samples.

Fig. 12 shows the absorption spectrum of the CdO and Co-doped CdO samples in the UV-visible range of 350–900 nm, it can be observed that as the doping amount of Co increase, the intensity of the spectra peaks decreases, and the peaks shift towards higher energy side (blue shift). A well-known way to estimate the direct and indirect band gap energies of metal oxides semiconductors is Tauc plot method [41, 42]. However, Another reported method in the literature [43-47] to accurately evaluates the band gap is to use the numerical first derivative of the absorption spectra with respect to phonon energy as shown in the inset of Fig. 12. In this case, the energy gap is an obvious inflection point in the top of the spectrum (maximum at lowest energy). Thus, the estimated band gap spectra of $Cd_{1-x}Co_xO$ (x = 0, 0.025, 0.05, 0.075, and 0.10) samples are 2.11, 2.22, 2.23, 2.42 and 2.50 eV, respectively. The estimated band gap of CdO with matched well with the previous reported value [48-50]. This blue shift or band gap broadening with increasing of cobalt doping can be interpreting in terms of quantum confinement on the electronic band structure of CdO nanocrystals. The quantum confinement became very apparent in nano-size, and similar behavior was observed in other studies [46, 51, 52]. But, strong quantum confinement effect can happen, if the crystal size of CdO is much smaller than the size of Bohr exciton radius [52-54]. However, the bulk Bohr radius of CdO is not available until now in the literature and the crystal size of CdO and doped CdO calculated from XRD and TEM are in the range of about 18nm. So, it is difficult to say for sure that the reason for the blue shift is due to quantum confinement of CdO nanoparticles. Another mechanism, which can explain this behavior, is the Moss-Burstein shift. This effect originates from the up-shift of the Fermi level in the conduction band when the carrier concentration increase [55, 56]. Fig. 13 shows the blue shift of the estimated energy gap with the increase of Co concentration of $Cd_{1-x}Co_xO$ samples.

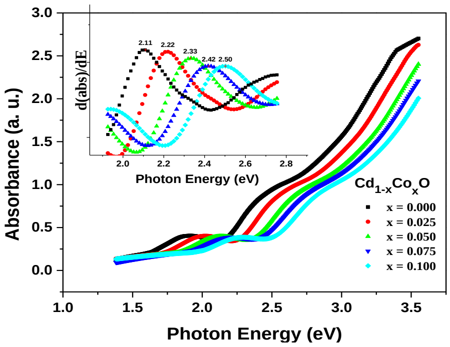

Fig. 12. Optical absorbance as a function of the photon energy measurements in the $Cd_{1-x}Co_xO$ nanoparticle. The inset shows the absorbance first derivative with respect to photon energy.

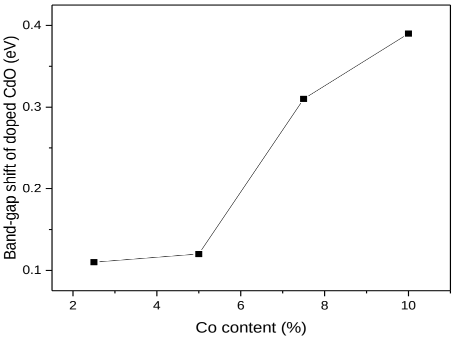

Fig. 13. Band-gap shift of doped CdO powder as a function of cobalt percent in CdO.

4. Conclusions

Co-doped CdO nanoparticles successfully synthesized via co-precipitation method. The TGA XRD and FT-IR techniques confirmed the pure and crystalline form of CdO and Co-doped CdO. Co-dopant has a demonstrable effect on the structural and physical properties of CdO. By increasing the cobalt concentration, both the crystal size and the microstrain decrease. Moreover, the preferred orientation of (111) plane, remain the same but the dislocation density increases. In addition, the UV-Vis spectra analysis concluded that the energy gap increases with the increase of Co-dopant ratio.

Acknowledgment

The authors are grateful to Al-Azhar and Aswan universities for supporting with experimental measurements and the authors also thank the Deanship of Scientific Research at King Khalid University (KKU) for funding this research project, Number: (R.G.P2/22/40) under research center for advanced material science.

References

[1] Z. Qiao, C. Agashe, D. Mergel, Thin Solid Films **496**, 520 (2006).
[2] S. Jäger, B. Szyszka, J. Szczyrbowski, G. Bräuer, Surface and Coatings Technology **98**, 1304 (1998).
[3] D. S. Raj, T. Krishnakumar, R. Jayaprakash, T. Prakash, G. Leonardi, G. Neri, Sensors and Actuators B: Chemical **171**, 853 (2012).
[4] P. H. Jefferson, S. Hatfield, T. D. Veal, P. King, C. F. McConville, J. Zúñiga–Pérez, V. Muñoz–Sanjosé, Applied Physics Letters **92**, 022101 (2008).
[5] A. Cimino, M. Marezio, Journal of Physics and Chemistry of Solids **17**, 57 (1960).
[6] R. Haul, D. Just, Journal of Applied Physics **33**, 487 (1962).
[7] F. Koffyberg, Journal of Solid State Chemistry **2**, 176 (1970).
[8] D. Kammler, T. O. Mason, D. Young, T. Coutts, Journal of Applied Physics **90**, 3263 (2001).
[9] M. Yan, M. Lane, C. Kannewurf, R. Chang, Applied Physics Letters **78**, 2342 (2001).
[10] H. Çolak, O. Türkoğlu, Materials Science in Semiconductor Processing **16**, 712 (2013).
[11] J. Santos-Cruz, G. Torres-Delgado, R. Castanedo-Pérez, S. Jiménez-Sandoval, J. Márquez-Marín, O. Zelaya-Angel, Solar energy materials and solar cells **90**, 2272 (2006).
[12] C. Ferekides, R. Mamazza, U. Balasubramanian, D. Morel, Thin Solid Films **480**, 224 (2005).
[13] C. Xiangfeng, Materials Research Bulletin **38**, 1705 (2003).
[14] M. Ristić, S. Popović, S. Musić, Materials Letters **58**, 2494 (2004).
[15] A. Gulino, G. Compagnini, A. A. Scalisi, Chemistry of Materials **15**, 3332 (2003).
[16] R. Fahim, G. Kolta, The Journal of Physical Chemistry **74**, 2502 (1970).
[17] A. Askarinejad, A. Morsali, Materials Letters **62**, 478 (2008).
[18] A. Hosseinian, A. R. Mahjoub, M. Movahedi, Journal of Applied Chemical Researches **4**, 43 (2010).
[19] J. B. Nelson, D. Riley, Proceedings of the Physical Society **57**, 160 (1945).
[20] E.R. Shaaban, M. El-Hagary, E.S. Moustafa, H.S. Hassan, Y.A.M. Ismail, M. Emam-Ismail, A.S. Ali, Applied Physics A: Materials Science and Processing 122, 1 (2016).

[21] A. Stokes, A. Wilson, Proceedings of the Physical Society **56**, 174 (1944).

[22] G. Williamson, W. Hall, Acta Metallurgica **1**, 22 (1953).
[23] Y. Rosenberg, V. S. Machavariani, A. Voronel, S. Garber, A. Rubshtein, A. Frenkel, E. Stern, Journal of Physics: Condensed Matter **12**, 8081 (2000).
[24] J.-M. Zhang, Y. Zhang, K.-W. Xu, V. Ji, Materials Letters **62**, 1328 (2008).
[25] D. Strauch, CdO: elastic constants: Datasheet from Landolt-Börnstein - Group III Condensed Matter · Volume 44E: "New Data and Updates for several III-V (including mixed crystals) and II-VI Compounds" in SpringerMaterials (https://dx.doi.org/10.1007/978-3-642-23415-6_59), in: U. Rössler (Ed.), Springer-Verlag Berlin Heidelberg.
[26] A. Kelly, K. M. Knowles, Crystallography and Crystal Defects, Wiley, 2012.
[27] J. I. Langford, KXDKKKKKKKKKCCIC Stalick, 3, ` (1992) RRRRRRREAAR5S.
[28] D. B. Williams, C.B. Carter, The transmission electron microscope, Transmission electron microscopy, Springer, 1996, pp. 3-17.
[29] T. Ungár, G. Tichy, J. Gubicza, R. Hellmig, Powder Diffraction **20**, 366 (2005).
[30] J. Gubicza, T. Ungár, Zeitschrift für Kristallographie-Crystalline Materials **222**, 567 (2007).
[31] J. Gubicza, Defect structure in nanomaterials, Elsevier, 2012.

[32] T. Kolonits, P. Jenei, B. G. Tóth, Z. Czigány, J. Gubicza, L. Péter, I. Bakonyi, Journal of The Electrochemical Society **163**, D107-D114 (2016).

[33] K. Anandhan, R. Thilak Kumar, Spectrochimica Acta Part A: Molecular and Biomolecular Spectroscopy **149**, 476 (2015).

[34] M. Arshad, A. Azam, A. S. Ahmed, S. Mollah, A. H. Naqvi, Journal of Alloys and Compounds **509**, 8378 (2011).

[35] S. Zandi, P. Kameli, H. Salamati, H. Ahmadvand, M. Hakimi, Physica B: Condensed Matter, **406**, 3215 (2011).

[36] M. Ashokkumar, S. Muthukumaran, Optical Materials **37**, 671 (2014).

[37] D. DurgaVijaykarthik, M. Kirithika, N. Prithivikumaran, N. Jeyakumaran, International Journal of Nano Dimension **5**, 557 (2014).

[38] A. Barve, S. Gadegone, M. Lanjewar, R. Lanjewar, Int. J. Recent Innov. Trends Comput. Commun. **2**, 2806 (2014).

[39] A. S. Lanje, R. S. Ningthoujam, S. J. Sharma, R. B. Pode, Luminescence and electrical resistivity properties of cadmium oxide nanoparticles, (2011).

[40] D. W. Sheibley, M. H. Fowler, Technical note. United States. National Aeronautics and Space Administration, (1967) 1-62.

[41] J. Tauc, A. Menth, States in the gap, Journal of Non-Crystalline Solids **8**, 569 (1972).

[42] N. Mott, E. Davis, Electron Processes in Non-Crystalline Materials, 1979, Clarendon, Oxford.

[43] M. Becerril, H. Silva-Lopez, O. Zelaya-Angel, Revista Mexicana de Física **50**, 588 (2004).

[44] I. L. Validžić, N. D. Abazović, M. Mitrić, M. V. Lalić, Z. S. Popović, F. R. Vukajlović, Journal of Nanoparticle Research **15**, 1347 (2013).

[45] A. E. Morales, E. S. Mora, U. Pal, Revista Mexicana de Fisica S **53**, 18 (2007).

[46] B. Potter Jr, J. Simmons, Journal of Applied Physics **68**, 1218 (1990).

[47] O. Zelaya- Angel, J. Alvarado- Gil, R. Lozada- Morales, H. Vargas, A. Ferreira da Silva, Applied Physics Letters **64**, 291 (1994).

[48] Cadmium oxide (CdO) energy gap: Datasheet from Landolt-Börnstein - Group III Condensed Matter · Volume 41B: "II-VI and I-VII Compounds; Semimagnetic Compounds" in SpringerMaterials (http://dx.doi.org/10.1007/10681719_508), in: O. Madelung, U. Rössler, M. Schulz (Eds.), Springer-Verlag Berlin Heidelberg, 1999.

[49] C. Bhosale, A. Kambale, A. Kokate, K. Rajpure, Materials Science and Engineering: B **122**, 67 (2005).

[50] R. Deokate, S. Salunkhe, G. Agawane, B. Pawar, S. Pawar, K. Rajpure, A. Moholkar, J. Kim, Journal of Alloys and Compounds **496**, 357 (2010).

[51] U. Desnica, M. Buljan, I. Desnica-Frankovic, P. Dubcek, S. Bernstorff, M. Ivanda, H. Zorc, Nuclear Instruments and Methods in Physics Research Section B: Beam Interactions with Materials and Atoms **216**, 407 (2004).

[52] A. Rastogi, S. Sharma, S. Kohli, Semiconductor science and technology **15**, 1011 (2000).

[53] L. E. Brus, The Journal of Chemical Physics **80**, 4403 (1984).

[54] A. D. Yoffe, Advances in Physics **42**, 173 (1993).

[55] T. Moss, Proceedings of the Physical Society. Section B **67**, 775 (1954).

[56] E. Burstein, Physical Review **93**, 632 (1954).